

Enhanced Light Utilization in Semitransparent Organic Photovoltaics Using an Optical Outcoupling Architecture

Yongxi Li, Chengang Ji, Yue Qu, Xinjing Huang, Shaocong Hou, Chang-Zhi Li, Liang-Sheng Liao, L. Jay Guo,* and Stephen R. Forrest*

Building-integrated photovoltaics employing transparent photovoltaic cells on window panes provide an opportunity to convert solar energy to electricity rather than generating waste heat. Semitransparent organic photovoltaic cells (ST-OPVs) that utilize a nonfullerene acceptor-based near-infrared (NIR) absorbing ternary cell combined with a thin, semitransparent, high conductivity Cu-Ag alloy electrode are demonstrated. A combination of optical outcoupling and antireflection coatings leads to enhanced visible transmission, while reflecting the NIR back into the cell where it is absorbed. This combination of coatings results in doubling of the light utilization efficiency (*LUE*), which is equal to the product of the power conversion efficiency (*PCE*) and the average photopic transparency, compared with a conventional semitransparent cell lacking these coatings. A maximum $LUE = 3.56 \pm 0.11\%$ is achieved for an ST-OPV with a $PCE = 8.0 \pm 0.2\%$ at 1 sun, reference AM1.5G spectrum. Moreover, neutral colored ST-OPVs are also demonstrated, with $LUE = 2.56 \pm 0.2\%$, along with Commission Internationale d'Éclairage chromaticity coordinates of $CIE = (0.337, 0.349)$ and a color rendering index of $CRI = 87$.

Moving global energy consumption away from fossil fuels toward renewable sources is a necessary step in reducing the rate of climate change. Among the many renewable energy sources available, solar energy is delivering on its promise of over 60 years as it increasingly becomes a source of low cost, clean, and literally infinite supply of clean energy. However, the current installed area of photovoltaic technologies only provides $\approx 2\%$ of the worldwide energy demand.^[1,2] The main obstacle to further growth of the solar energy market is the cost and rate of

installation of solar panels. The development of building-integrated photovoltaics (BIPVs) that integrate transparent solar cells onto window panes, skylights, and building facades provides an emerging opportunity for installation of solar cells in locales that have yet to be fully exploited for this purpose.^[3–13]

Semitransparent Si solar cells on glass can generate energy along with partial interior shading.^[14] However, the broad visible light absorption spectra of inorganic solar cells limit their potential utility in BIPV applications. In this regard, semitransparent organic photovoltaics (ST-OPVs) provide an attractive alternative due to their narrow excitonic absorption spectra that can allow for visible light transmission along with ultraviolet (UV)/near-infrared (NIR) absorption through the choice of molecular composition of the device active region.^[15] Using such an approach, both high power conversion

efficiency (*PCE*) and visible transmittance can be simultaneously achieved.^[16–25] Moreover, mechanical flexibility, pleasant appearance, and light weight enhance their potential utility for BIPV applications.^[26]


Unlike conventional photovoltaics, semitransparent cells can be an effective solution for balancing energy generation with accurately transmitting the solar spectrum. To accurately quantify their performance in addition to *PCE*, the apparent transparency of a window known as the average photopic transmittance (*APT*), needs to be optimized (see the Experiment Section). Thus, the light utilization efficiency ($LUE = PCE \times APT$) provides a useful figure of merit of ST-OPV performance, which enables comparison between technologies and also represents an overall system efficiency that incorporates both the generated power efficiency and overall lighting efficiency.^[1] Although recent rapid developments of small energy gap materials provide opportunities to achieve efficiency $>9\%$ for semitransparent OPVs, most devices demonstrated to date exhibit $APT \approx 30\%$, giving $LUE < 3.0\%$ (see Figure S1 in the Supporting Information for a compilation of recent results), due to the inevitable trade-off between the *PCE* and *APT*.

In addition to the pursuit of high *PCE* and *APT*, the *appearance* of power generating windows is equally important. One note of caution in reading the data in Figure S1 (Supporting Information) is that not all cells are neutral density. This is particularly true for the organic and perovskite cells that can

Y. Li, C. Ji, Y. Qu, X. Huang, S. Hou, Prof. L. J. Guo, S. R. Forrest
Departments of Electrical Engineering and Computer Science
University of Michigan
Ann Arbor, MI 48109, USA
E-mail: guo@umich.edu; stevefor@umich.edu, forrest@princeton.edu

Prof. C.-Z. Li
Department of Polymer Science and Engineering
Zhejiang University
Hangzhou 310027, P. R. China

Prof. L.-S. Liao
Institute of Functional Nano & Soft Materials (FUNSOM)
Soochow University
Suzhou, Jiangsu 215123, P. R. China

 The ORCID identification number(s) for the author(s) of this article can be found under <https://doi.org/10.1002/adma.201903173>.

DOI: 10.1002/adma.201903173

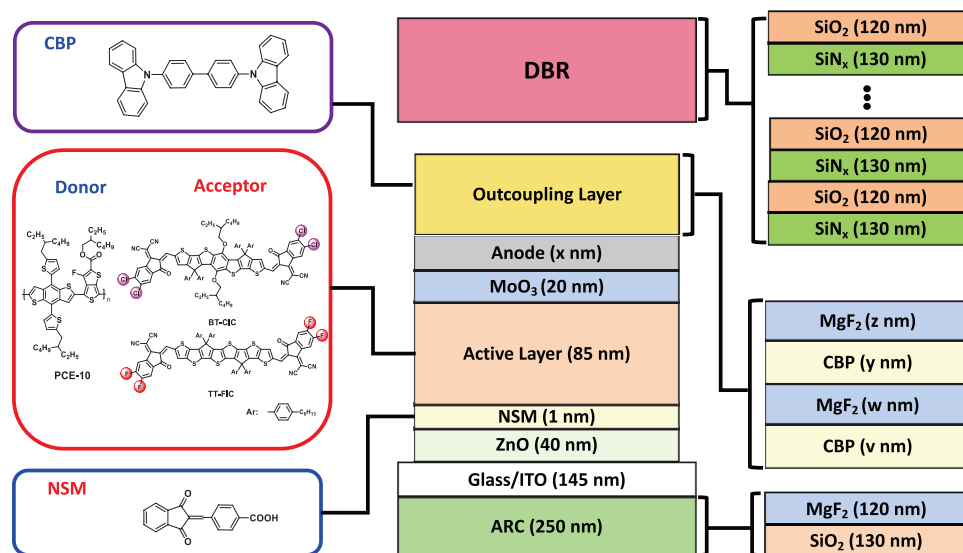


Figure 1. Schematic of the semitransparent device showing optimized layer thicknesses and compositions. Left: molecular structural formulae of the NSM, CBP, donors (PCE-10), and acceptors (TT-FIC and BT-CIC). Right: detailed layer structures of the outcoupling layer, antireflection layer, and distributed Bragg reflector.

have noticeable tints. If the coloration is too strong, the cells no longer perform as windows, but rather as power generating “optical filters” that do not serve the purpose of building integrated appliances.

Here, unlike conventional ST-OPVs where the enhancement in *LUE* primarily originates from recycling the NIR photons back into the active region using combination of an antireflection coating (ARC) and a mirror in the NIR,^[4] we show that the appearance and efficiency of the ST-OPVs can simultaneously be tailored by applying a second coating on the exit surface, called an *outcoupling* (OC) layer. Combining the elements of near-infrared (NIR) absorbing materials sets with a semitransparent, sputtered 2% Cu-Ag alloy electrode, as well as multilayer ARC and OC layers, results in $LUE = 3.56 \pm 0.11\%$, with $PCE = 8.0 \pm 0.2\%$ and $APT = 44.2 \pm 1.4\%$. Also, a neutral-color ST-OPV with $LUE = 2.56 \pm 0.2\%$, and $APT = 44.3 \pm 1.5\%$ is demonstrated with Commission Internationale d'Éclairage chromaticity coordinates of $CIE = (0.337, 0.349)$ and a color rendering index of $CRI = 87$ when illuminated by a reference AM1.5G solar spectrum.

Figure 1 shows a schematic illustration of the ST-OPV structure. The inverted device employs an OC on the semitransparent contact, and an ARC on the back surface of the glass substrate. The OC has the effects of increasing the transmission and reducing reflections in the visible while reflecting the NIR radiation back into the device active region. The ARC reduces optical reflections at the glass-air interface, thus increasing the total transmission in the visible. The DBR is grown on a separate quartz substrate works as both a NIR mirror and an encapsulating lid to prevent oxygen and moisture from degrading the device. The photoactive layer comprises two solution-processed NIR absorbing nonfullerene acceptors (TT-FIC, BT-CIC), and a polymer donor (PCE-10) forming a ternary blend bulk heterojunction (TBHJ).^[27] Thin film absorption spectra of PCE-10, BT-CIC, and TT-FIC are shown in **Figure 2a**. The molecular structural formulae of the molecules are shown

in **Figure 1** and their nomenclatures are provided in the Experimental Section.

The semitransparent Cu-Ag alloy anode consists of 2% Cu in Ag deposited by cosputtering. The Cu atoms act as nucleation sites for Ag atoms, thus preventing Ag aggregation. As a result, continuous Cu-Ag films are achieved at thicknesses of only 8 nm, compared with 15 nm required for a neat Ag layer (the series and sheet resistances increase significantly with thickness below 15 nm.). Details of optimization can be found in **Figure S2** (Supporting Information). The 2% Cu-Ag alloy shows the lowest imaginary part (ϵ_2) of the permittivity across the entire wavelength range, which is favorable for achieving high transparency. The transmission spectra of three different ultrathin metal films (Ag, Ag with Au seed layer, and Cu-Ag) are shown in **Figure 2b**. The Cu-Ag film shows the highest average transmittance in the visible, with $T_{\text{avg}} = 72 \pm 3\%$ calculated from the arithmetic mean of the transmittances from 400 to 650 nm. The transmittances for Ag and Au-Ag are lower, at $T_{\text{avg}} = 58 \pm 2\%$ and $T_{\text{avg}} = 64 \pm 2\%$, respectively. The strong visible absorption of Au results in the reduced T_{avg} for Au-Ag, whereas aggregation of Ag leads to reduced transparency in the neat film. As shown in **Figure 2c–e**, the Ag film has a root-mean-square roughness of $RMS = 6.25 \pm 0.3$ nm. The formation of Ag islands introduces plasmon losses of the incident light, resulting in reduced transmittance. In contrast, $RMS = 0.70 \pm 0.04$ nm for an 8 nm thick Cu-Ag film, and $RMS = 1.54 \pm 0.08$ nm for Au-Ag films of comparable thickness. Furthermore, the sheet resistances of both Cu-Ag and Au-Ag are $11.3 \pm 0.5 \Omega \text{ sq}^{-1}$ compared with $26.9 \pm 1.3 \Omega \text{ sq}^{-1}$ for Ag.

The current-density–voltage (J – V) characteristics and external quantum efficiency (*EQE*) spectra for the ST-OPVs using Cu-Ag, Au-Ag, and Ag anodes are shown in **Figures S3** and **S4** (Supporting Information), with a summary of device performance given in **Table 1** and **Table S1** (Supporting Information). We also prepared a cell with a thick Ag anode with the structure: ITO/ZnO (40 nm)/NSM (1 nm)/ PCE-10:BT-CIC:TT-FIC

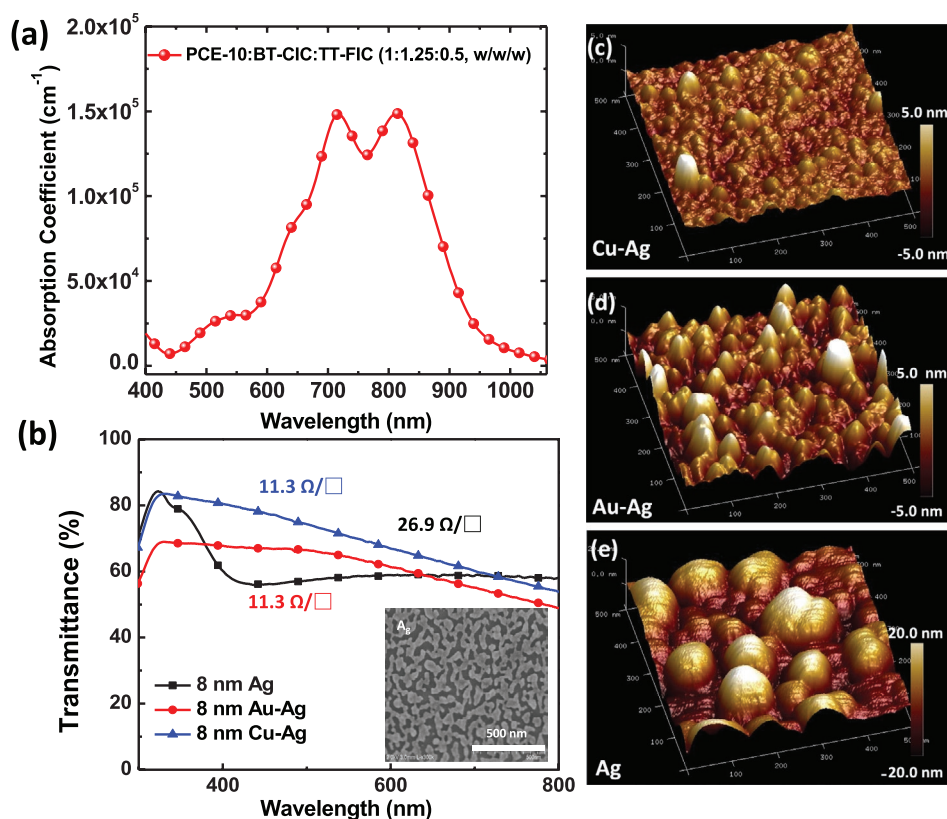


Figure 2. a) UV-vis absorption spectra of PCE-10, BT-CIC, and TT-FIC blend films. b) Optical transmission characteristics of the semitransparent cells with different anodes at the thickness of 8 nm. Inset: scanning electron microscope (SEM) image of a pure Ag film (8 nm). c) Atomic force microscopy (AFM) topographic images (500 × 500 nm) of the c) Cu-Ag (8 nm), d) Au-Ag (8 nm), and e) Ag (8 nm) films.

(1:1.25:0.5, 85 nm)/MoO₃ (20 nm)/Ag (100 nm) to study the tradeoff between transparency and efficiency. Compared to the opaque device, the semitransparent devices with the Cu-Ag alloy anode show a decreased J_{SC} , but similar V_{OC} and FF . The lower J_{SC} is due to the reduced reflectivity of the thin anode leading to reduced light absorption within the active layer. The APT and PCE of these devices vary from $APT = 17.8 \pm 0.5\%$ and $PCE = 8.6 \pm 0.3\%$, to $APT = 35.4 \pm 1.3\%$ and $PCE = 7.2 \pm 0.3\%$, with a Cu-Ag thickness of $21 \text{ nm} \geq x \geq 11 \text{ nm}$. For $x = 11 \text{ nm}$, the ST-OPV has $LUE = 2.55 \pm 0.07\%$, and for $x = 16$ and 21 nm ,

$LUE = 2.07 \pm 0.06\%$ and $1.53 \pm 0.05\%$, respectively. To avoid overestimation of J_{SC} measured using a solar simulator, the J_{SC} reported here are values integrated from the measured EQE spectra.^[28]

Although $PCE = 8.6\%$ was obtained in these ST-OPVs, the low APT strongly limits their development, since architectural glass requires an $APT \approx 50\%$.^[1] To solve this problem, an OC consisting of four layers: CBP ($v \text{ nm}$, index of refraction, $n_{CBP} = 1.90 \pm 0.03$ /MgF₂ ($w \text{ nm}$, $n_{MgF_2} = 1.38 \pm 0.01$)/CBP ($y \text{ nm}$)/MgF₂ ($z \text{ nm}$) is deposited onto the Cu-Ag surface to maximize visible

Table 1. Operating characteristics of semitransparent OPVs under simulated AM 1.5G, 100 mW cm⁻² illumination.

Device*	$J_{SC, EQE}^a$ [mA cm ⁻²]	V_{OC} [V]	FF	PCE^b [%]	APT [%]	LUE [%]	CEI
100 nm Ag	23.3 ± 0.4	0.68 ± 0.01	0.72 ± 0.01	11.4 ± 0.3	–	–	–
11 nm Cu-Ag	15.0 ± 0.4	0.68 ± 0.01	0.71 ± 0.01	7.2 ± 0.3	35.4 ± 1.3	2.62 ± 0.07	(0.276, 0.314)
11 nm Cu-Ag (with OC and ARC)	14.8 ± 0.3	0.67 ± 0.01	0.72 ± 0.01	7.2 ± 0.2	49.0 ± 1.5	3.53 ± 0.10	(0.291, 0.332)
16 nm Cu-Ag	16.6 ± 0.3	0.68 ± 0.01	0.72 ± 0.01	8.1 ± 0.2	25.6 ± 1.0	2.07 ± 0.06	(0.256, 0.287)
16 nm Cu-Ag (with OC and ARC)	16.2 ± 0.2	0.68 ± 0.01	0.72 ± 0.01	8.0 ± 0.2	44.2 ± 1.4	3.56 ± 0.11	(0.280, 0.335)
21 nm Cu-Ag	17.9 ± 0.4	0.68 ± 0.01	0.71 ± 0.01	8.6 ± 0.3	17.8 ± 0.5	1.53 ± 0.05	(0.243, 0.262)
21 nm Cu-Ag (with OC and ARC)	18.0 ± 0.4	0.68 ± 0.01	0.72 ± 0.01	8.8 ± 0.3	35.6 ± 1.3	3.13 ± 0.09	(0.258, 0.328)

^aThe J_{SC} values are calculated from the integral of the EQE spectrum; ^bThe PCE are calculated based on measurement of eight devices.

transmission of the ST-OPVs. The ST-OPV with a $x = 16$ nm Cu-Ag anode is used to illustrate the function of this layer. The same design principle can be extended to other devices using electrodes with different thicknesses.

Transmission resonance occurs when the net phase shift equals $2n\pi$ (n is an integer). On the other hand, the reflection resonances occur when the net phase shift is equal to $(2n + 1)\pi$. Therefore, control of the phase shift by changing the thickness of CBP and MgF_2 can maximize the transmission resonance in the visible while reflection is maximized in the NIR. Figure S5a (Supporting Information) shows the optical field intensity within the OC device versus wavelength. The OC has increased transmission between 400 and 600 nm with a peak at 555 nm, which is consistent with the transmission spectra in Figure S5b (Supporting Information). Figure S6 (Supporting Information) shows the net phase shift, which includes phase shifts acquired upon reflection from both the top and bottom interfaces, and the propagation phase accumulated within each layer of the device. Intensity maxima are apparent at 554 nm with 40 nm CBP, at 555 nm with 100 nm MgF_2 , 557 nm with 70 nm CBP, and at 568 nm with 40 nm MgF_2 . Similarly, the reflection resonances are realizing around 800 nm. Therefore, illumination at $\lambda > 700$ nm is recycled into the active layer by the OC, which results in an increased absorption in the range of 700–1000 nm.

ST-OPVs with OC layers were fabricated with the structure: (ITO)/ZnO (40 nm)/NSM (1 nm)/PCE-10:BT-CIC:TT-FIC (1:1.25:0.5, 85 nm)/ MoO_3 (20 nm)/Cu-Ag (16 nm)/CBP (40 nm)/ MgF_2 (100 nm)/CBP (70 nm)/ MgF_2 (40 nm), as shown in Figure 3a. The ST-OPV with an OC shows that the *APT*

increases from $25.6 \pm 0.1\%$ to $42.6 \pm 1.3\%$, nearly 61% improvement than that of a cell without an OC layers, which in agreement with simulations (see Figure 3b,c). An ARC consisting of a bilayer of 120 nm thick MgF_2 and 130 nm low refractive index SiO_2 ($n_{\text{SiO}_2} = 1.12 \pm 0.03$) was deposited onto the distal surface of the glass substrate to further reduce optical reflections at the glass–air interface.^[29] As shown in Figure 3d, The ARC-coated ST-OPV shows a reduced reflection from $\approx 10\%$ at 500 nm to $\approx 6\%$, thus leading to an increase in *APT* = $44.2 \pm 1.4\%$.

Figure 4 shows the *J-V* and *EQE* characteristics of optimized ST-OPVs with both OC and ARC together with their transmission and reflection spectra. The incorporation of the OC and ARC significantly increases visible transmission and reduces reflections for all three transparent devices. It is worth noting that the *PCEs* maintain their initial values along with an increase in visible transmittance, thus further improving the *LUE*. The *APT* varies from $49.0 \pm 1.5\%$ to $35.6 \pm 1.3\%$, for $x = 11$ nm to 21 nm, respectively. For $x = 11$ nm, the *PCE* = $7.2 \pm 0.2\%$ and *LUE* = $3.53 \pm 0.10\%$, and for $x = 16$ and 21 nm, *PCE* = $8.0 \pm 0.2\%$ and $8.8 \pm 0.3\%$, *LUE* = $3.56 \pm 0.11\%$ and $3.13 \pm 0.09\%$, respectively. Furthermore, an increased *EQE* in the range of 700–1000 nm is achieved with the OC and ARC that increase absorption at long wavelengths as result of increasing backside NIR reflections from the OC, and reduced NIR reflections at the front-side contact from the ARC. The ST-OPV (16 nm Cu-Ag) optical properties are dependent on light incidence angle $< 60^\circ$ from normal. For example, chromaticity changes from (0.280, 0.335) at 0° , to (0.273, 0.332), (0.253, 0.316), and (0.244, 0.282) at 20° , 40° , and 60° , respectively (see Figure S7, Supporting Information).

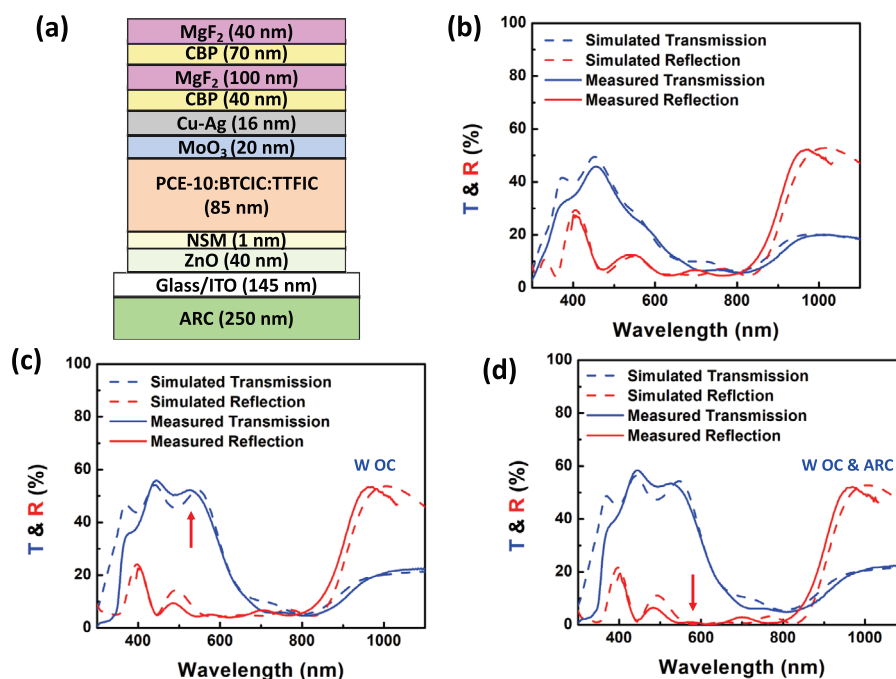


Figure 3. a) Schematic of the semitransparent device (16 nm Cu-Ag) showing optimized layer thicknesses and compositions with both outcoupling (OC) and antireflection (AR) coatings. Measured and simulated reflection and transmission spectra of the semitransparent devices b) without OC and AR coatings, c) with only OC coatings, and d) with both OC and AR coatings.

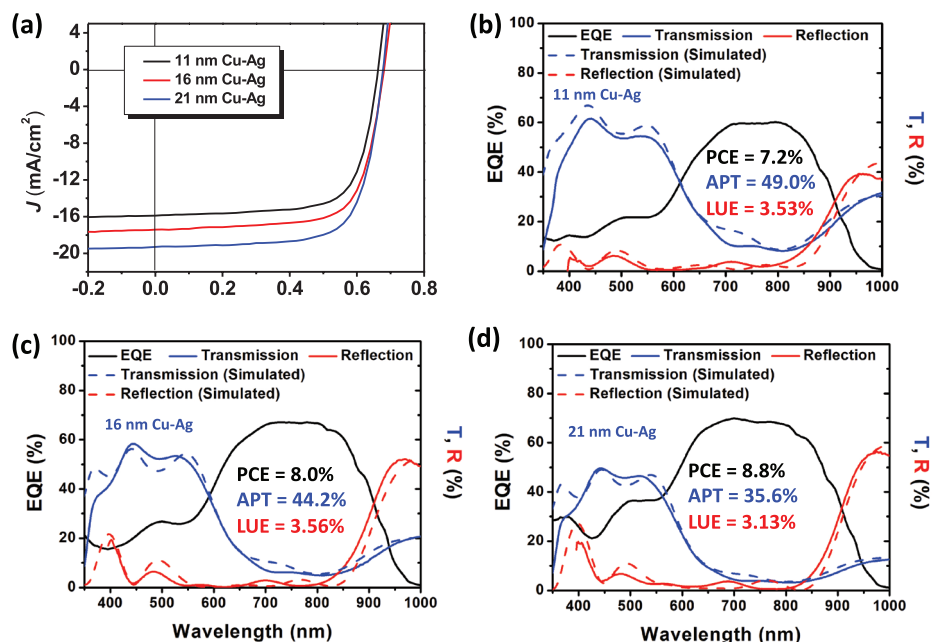


Figure 4. a) Current density–voltage characteristics of the optimized semitransparent cells with different anode thicknesses. Measured and simulated optical transmission, reflection, and external quantum efficiencies of the semitransparent cells b) with 11 nm Cu-Ag, c) with 16 nm Cu-Ag, and d) with 21 nm Cu-Ag anode.

In previous work, a distributed Bragg reflector (DBR) was used to increase the NIR photon harvesting for devices with semitransparent top electrodes.^[4,7,30] Here, we employed a similar strategy by growing a DBR mirror on a separate quartz substrate comprising 12.5 alternating layers of plasma enhanced chemical vapor deposited SiN_x and SiO₂. As shown in Figure S8 (Supporting Information), the DBR exhibited over 98% reflectance between 650 and 850 nm, which matched the absorption of the PCE-10:BT-CIC:TT-FIC (1:1.25:0.5) blend. Using the mirror, the ST-OPV devices showed further increases in *PCE* ($7.2 \pm 0.2\%$ vs $7.4 \pm 0.3\%$ for 11 nm Cu-Ag device, $8.0 \pm 0.2\%$ vs $8.2 \pm 0.3\%$ for 16 nm Cu-Ag device) due to increased photocurrent generation in the NIR absorbing device. Note that the attachment of a separately fabricated mirror only slightly increases device complexity (see Table S2, Supporting Information).

Finally, we demonstrated color-neutral ST-OPVs employing OC layers. An 8 nm thick Cu-Ag layer is selected as the anode to enhance the device transparency. A bilayer structure consisting of CBP and ZnS, that excites additional transmission resonances near 600 nm, is introduced to balance the blue transmission of device (Figure S9, Supporting Information). The device with an 8 nm thick Cu-Ag anode exhibits a lower *LUE* = $2.56 \pm 0.2\%$ compared to the device with 16 nm Cu-Ag and a CBP/MgF₂ OC layer with *LUE* = 3.56%. However, its 1931 CIE chromaticity coordinates (0.337, 0.349, see Figure 5a) are close to the AM1.5G solar spectrum point (0.332, 0.343). This ST-OPV achieves a color rendering index of *CRI* = 87 and a correlated color temperature of *CCT* = 5310 K. This indicates that the illumination through the OPV window accurately renders the color of an object. Moreover, the transmission spectra are only weakly dependent on illumination angle up to 60° from normal (see Figure S10, Supporting Information). A

comparison of the performance of the two, near-neutral density devices is given in Table 2. Also, red, green, and blue (R, G, B) tinted ST-OPVs are demonstrated by tailoring the design of OC layers (see Figure S11 and Table S3, Supporting Information). These tinted devices might have potential applications in aesthetically fashioned buildings to create a desired visual appearance. Although the energy harvesting for building integration will vary depending on location (from Equator to Arctic) and time of day, specific device structures and/or optical designs for each location can be optimized reduce or eliminate oblique angle variations in light harvesting.^[31]

ST-OPVs require that the active materials absorb in the NIR, and the low resistance contacts themselves must also be optically transmissive. Indium tin oxide (ITO) is almost universally used as bottom electrode due to its high transparency, relatively low resistance and high work function. However, utilization of ITO as a top electrode remains a challenge due to damage of the underlying organic layers during its sputter deposition. Solution processable electrodes based on metal nanowires,^[32–34] nanotubes^[35,36] and graphene^[37,38] are promising alternatives, but their performance remains inferior to metals, and even ITO as anode materials. In contrast, thermally evaporated or sputtered ultrathin metal films have the best combination of transparency and conductivity. A 15 nm thick semitransparent Ag electrode, for example, shows a sheet resistance of $\approx 4.3 \Omega \text{ sq}^{-1}$, with a peak transmittance of 76% at 425 nm, decreasing to a minimum of 40% at 650 nm. As mentioned above, a few nanometers of Ag tends to form isolated nuclei that limit transparency and increase resistance. In our work, we minimize cluster formation by using a sputtered, 2% Cu-Ag alloy anode. This alloy composition results in a uniform layer as thin as 8 nm with a transmittance of 70–80% across the visible, while exhibiting a lower sheet resistance of only $11.3 \Omega \text{ sq}^{-1}$ compared to $26.9 \Omega \text{ sq}^{-1}$ for Ag film.

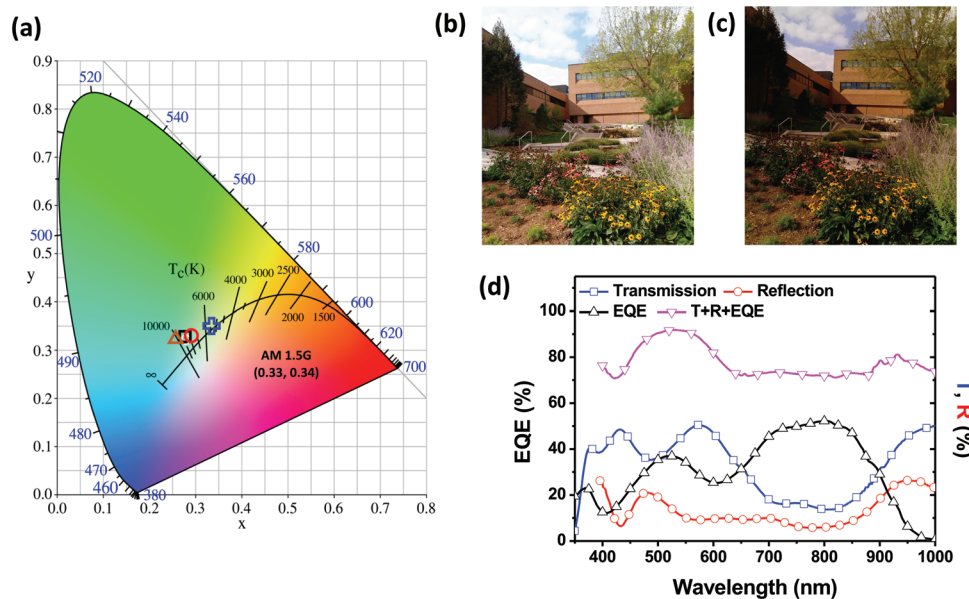


Figure 5. a) Chromaticity chart showing the CIE coordinates of the transmission spectra of the neutral color device (denoted by “+”), 11 nm thick Cu-Ag (square), 16 nm Cu-Ag (circle), and 21 nm Cu-Ag (triangle) using a reference AM1.5G solar input spectrum. b) Photograph of the outdoor image in comparison to c) a view through the neutral color cell (right). d) Measured optical transmission, reflection, external quantum efficiencies, and their sum of the neutral color device.

One of the most interesting challenges in thin film semitransparent solar cells is to balance *PCE* and *APT*, thus maximizing the *LUE*. Previous approaches have demonstrated that DBR mirrors^[4] or aperiodic dielectric reflectors (ADRs)^[7] can increase the *PCE* by recycling NIR photons back into the active region. In this work, we include a two-period, CBP/MgF₂ light outcoupling layer that reduces trapping of visible radiation within the cell and also increases the NIR reflectivity. This approach provides for freedom in varying the device architecture and the choice of active materials without altering the electrical characteristics of the device itself. Therefore, both the *PCE* and *APT* can be independently optimized to deliver the highest performance. The outcoupling layer has a narrow spectral bandwidth, and thus also can control the cell appearance.

It should be noted that we use *APT* instead of average visible transmittance (*AVT*) to quantify the transmittance of our cells. This is consistent with generally accepted practices of the window manufacturing industry that weight the integration of the transmission spectrum against the photopic response of the human eye.^[39] In some cases, there is a significant difference between the transmission spectra of the ST-OPVs and the photopic response of the human eye (see Figure S12, Supporting Information). Therefore, the *AVT* can lead to an

overestimation in the *perceived transparency* of the window. For example, in previous work there is a relative 10% difference between *AVT* = 43% and *APT* = 39%.^[18]

We demonstrated efficient ST-OPVs comprising an NIR-absorbing nonfullerene acceptor-based TBHJ along with a semitransparent, thin Cu-Ag alloy electrode. The cell absorbs between 600 and 1000 nm while leaving a transparent window in the range of 400–600 nm. The combined use of an OC and ARC increases visible transmission while enhancing the reflection in the NIR to improve the device efficiency. This approach allows freedom in varying the device architecture and the materials used without degrading the electrical characteristics of the device itself. With this strategy, we demonstrate an optimized ST-OPV cell with *PCE* = 8.0 ± 0.2%, *APT* = 44.2 ± 1.4% and *LUE* = 3.56 ± 0.11% which is twice that of a cell lacking these coatings. When utilizing a DBR mirror on top of semitransparent contact, the *PCE* was improved to 8.2 ± 0.3%. Furthermore, the neutral ST-OPV shows *PCE* = 5.8 ± 0.2%, and *APT* = 44.3 ± 1.5% with CIE coordinates of (0.337, 0.349) and *CRI* = 87. In a recent study of the theoretical efficiency limits of ST-OPVs, it was determined that cells with *APT* = 50% have the potential to exhibit a *PCE* close to 15%. Combining photonic control proposed here with new transparent electrode, as well as materials sets that absorb out to wavelengths of 1100 nm, we

Table 2. Operating characteristics of semitransparent, near-neutral OPVs.

Anode	J_{SC}^a [mA cm ⁻²]	V_{OC} [V]	<i>FF</i>	<i>PCE</i> ^b [%]	<i>APT</i> [%]	<i>LUE</i> [%]	<i>CIE</i> ^c	<i>CRI</i>	<i>CCT</i> [K]
8 nm Cu-Ag	13.2	0.65	0.67	5.8	44.3	2.56	(0.34, 0.35)	87	5310
16 nm Cu-Ag	16.6	0.68	0.72	8.0	44.2	3.56	(0.28, 0.34)	–	8250

^aThe J_{SC} values are calculated from the integral of the EQE spectrum; ^bThe *PCE* are calculated based on measurement of eight devices; ^cThe 1931 CIE chromaticity coordinates calculated using a reference AM1.5G solar spectrum.

expect the performance of ST-OPVs to approach these predicted efficiencies in the near future.

Experiment Section

Materials: All devices were grown on patterned ITO substrates with sheet resistances of $15 \Omega \text{ sq}^{-1}$. The acceptors, (4,4,10,10-tetrakis(4-hexylphenyl)-4,10-dihydrothieno[2'',3':4',5']thieno[3',2':4,5]cyclopenta[1,2-b]thieno[2,3-d]thiophene-2,8-diyl)bis(2-(3-oxo-2,3-dihydroinden-5,6-difluoro-1-ylidene)malononitrile), TT-FIC; (4,4,10,10-tetrakis(4-hexylphenyl)-5,11-(2-ethylhexyloxy)-4,10-dihydro-dithienyl[1,2-b:4,5b']benzodi-thiophene-2,8-diyl)bis(2-(3-oxo-2,3-dihydroinden-5,6-dichloro-1-ylidene)malononitrile)), BT-CIC, were synthesized in our group. 2-[4-(carboxyl)benzylidene]-1H-indene-1,3(2H)-dione (NSM) was synthesized by Li et al. Other materials were purchased from commercial suppliers: MoO₃ (Acros Organics), 4,4'-bis(*N*-carbazolyl)-1,1'-biphenyl (CBP, Luminescence Technology Corp.), MgF₂ (Kurt J. Lesker Corp.), and PCE-10 (1-Material).

Solar Cell Fabrication: Prepatterned ITO on glass substrates was cleaned using a series of detergents and solvents, and exposed to ultraviolet-ozone for 10 min before growth. The vacuum-deposited layers were grown at $\approx 1 \text{ \AA s}^{-1}$ in a high vacuum chamber with a base pressure of 2×10^{-7} torr. The vacuum chamber was connected to glove boxes filled with ultrapure N₂ (O₂, H₂O < 0.1 ppm). The ZnO layer (≈ 40 nm) was spin cast from a ZnO precursor solution onto the substrates and then thermally annealed at 150 °C for 30 min in air. The NSM was dissolved in methanol with a concentration of 1 mg mL⁻¹ and spin coated at 4000 rpm for 60 s, followed by thermal annealing at 100 °C for 10 min. The substrate was washed in methanol at 4000 rpm for 60 s. The active layer, PCE-10:BT-CIC:TT-FIC (1:1.25:0.5 w/w/w), was dissolved in chlorobenzene:chloroform (CB:CF, 9:1 by vol.) at a concentration of 16 mg mL⁻¹. The solution was stirred overnight on a hot plate at 65 °C, and then spin-coated at 2000 rpm for 90 s to achieve a thickness of 85 nm. The samples were then transferred back to the vacuum chamber for deposition of MoO₃.

All metal electrodes were deposited at room temperature by a DC magnetron sputtering at a chamber base pressure of 1×10^{-6} Torr. During the deposition, the substrate holder was rotated at a rate of 10 rpm. The Cu-Ag electrodes were deposited via cosputtering from Cu and Ag targets with the Ar pressure of 4.5 mTorr. The optical and electrical properties of the Cu-Ag films were optimized by adjusting the source powers for the targets, which correspondingly changed the film composition. The optimal deposition rates of Cu and Ag were 0.19 and 11.09 Å s⁻¹, respectively. For the Au-Ag films, the ≈ 1 nm thick Au seed layer was deposited at a rate of 8.3 Å s⁻¹ at an Ar pressure of 3.5 mTorr, and the top Ag was deposited at a rate of 12.4 Å s⁻¹ at 4.5 mTorr. Pure Ag electrodes were deposited at a rate of 12.4 Å s⁻¹ at 4.5 mTorr. The device areas of 4.0 mm² were defined by the overlap between the patterned ITO and the metal contact deposited through an ultrathin shadow mask (50 μm).

The OC was grown by vacuum thermal evaporation (VTE) at 1 Å s⁻¹ for MgF₂, and 0.6 Å s⁻¹ for CBP. ZnS was deposited by electron-beam at 3 Å s⁻¹ and a base pressure of 2×10^{-6} Torr. The thickness of each layer of the 11 nm Cu-Ag device was $\nu = 35$ nm, $w = 100$ nm, $\gamma = 70$ nm, and $z = 60$ nm. For the 16 and 21 nm Cu-Ag device: $\nu = 40$ nm, $w = 100$ nm, $\gamma = 70$ nm, $z = 40$ nm. Finally, the ARC was grown onto the glass substrate after the devices were complete. MgF₂ was deposited by VTE at a rate of 1 Å s⁻¹, while the SiO₂ was grown by electron beam deposition with the substrate at an angle of 85° to the beam direction to achieve a low refractive index of 1.1. A DBR, consisting 12.5 pairs of 130 nm SiN_x and 120 nm SiO₂ on a fused silica substrate, was grown by plasma-enhanced chemical vapor deposition at a rate of 5.2 Å s⁻¹ for SiN_x layer and 7.4 Å s⁻¹ for SiO₂ layer. The neutral density device structure is (ITO)/ZnO (40 nm)/PCE-10:BT-CIC:TT-FIC (1:1.25:0.5, 85 nm)/MoO₃ (10 nm)/Cu-Ag (8 nm)/CBP (140 nm)/ZnS (56 nm).

Solar Cell Characterization: The current-density–voltage (*J*–*V*) characteristics and EQE of the cells were measured in a glove box

filled with ultrapure N₂. The EQE measurements were performed with devices underfilled by a 200 Hz chopped monochromated and focused beam from a Xe lamp. The current output from the devices as well as from a reference NIST-traceable Si detector was recorded using a lock-in amplifier. Light from a Xe lamp filtered to achieve a simulated AM 1.5G spectrum (ASTM G173-03) was used as the source for *J*–*V* measurements. The mismatch calculated factors were between 1.006 and 1.009. The lamp intensity was varied using neutral density filters and was calibrated by a Si reference cell certified by National Renewable Energy Laboratory (NREL). Each cell was measured under six different light intensities from 0.001 to 1 sun (100 mW cm⁻²).

ST-OPVs were measured from the ITO side with an ultrathin metal mask (2.0 mm²) and no object behind the cells. Errors quoted account for measurement variations from three or more cells, as well as an additional systematic error of 5% for *J*_{SC} and *PCE*. The *J*–*V* characteristics of the ST-OPVs were reproducible from device to device and run to run, and were independent of the light exposure time (1–5 min). The cells were measured more than 3 months after fabrication, showing stable performance with little degradation (see Figure S13, Supporting Information). The devices were encapsulated, stored in air and kept in the dark between measurements. The data showed that the device is stable over the three months with $\approx 10\%$ reduction in *PCE*. Optical simulations and optimization of the single junction used MATLAB based on the transfer matrix method in combination with the measured *J*–*V* characteristics of each cell.

Optical and Electrochemical Characterization: The reflection spectra of fabricated devices were measured with a thin-film measurement instrument (F20, Filmetrics) integrated with a spectrometer and light source (395–1032 nm). The transmission spectra and layer thicknesses were measured with by spectroscopic ellipsometry (M-2000, J. A. Woollam Co.) with a beam diameter of ≈ 4 mm. The film absorbance was measured using UV–vis spectrometer (Perkin Elmer 1050). Optical simulations based on the transfer matrix method were performed to calculate the spectral reflection, absorption in the active layer and transmission, electric field intensity distributions, and phase shifts. The refractive indices of materials used in the simulations were measured by spectroscopic ellipsometry. The four-point probe method (FPP-5000, Miller Design & Equipment) was used for sheet resistance measurements.

The average photopic transmission (*APT*) is calculated using

$$APT = \frac{\int T(\lambda)P(\lambda)S(\lambda)d(\lambda)}{\int P(\lambda)S(\lambda)d(\lambda)} \quad (1)$$

where λ is the wavelength, *T* is the transmission, *P* is the normalized photopic spectral response of the eye, and *S* is the solar photon flux (AM1.5G).

Finally, one important consideration in reporting the performance of ST-OPV is photon balance, where the sum of the absorption (*A*), reflection (*R*), and transmission (*T*) of the device should be equal to 1 at every wavelength. Owing to difficulties in measuring *A* directly, the minimum absorption can be estimated from the EQE and the parasitic absorption of the electrode. In this approximation, the sum of EQE, *T*, and *R* should be less than unity at every wavelength. Recently, reports of ST-OPVs with very high *PCE* showed EQE+*T*+*R* > 1. This might be explained by errors in accounting for extrinsic absorption (i.e., by the ITO anode), or the device area was smaller than the beam spot. Therefore, independent EQE, *R*, and *T* measurements for each device are required to avoid these errors.

Data Availability: The data that support the plots within this paper and other findings of this study are available from the corresponding author upon reasonable request.

Supporting Information

Supporting Information is available from the Wiley Online Library or from the author.

Acknowledgements

Y.L. and C.J. contributed equally to this work. This work was supported by the SunShot Program of the Department of Energy under award number DE-EE0008561 (Y.L., experiment and analysis; S.R.F., analysis) and the Department of the Navy, Office of Naval Research under award no. N00014-17-1-2211 (Y.L. and Y.Q., experiment and analysis), Universal Display Corp., and MTRAC Advanced Materials Hub 2018 Award Program (C.J., experiment; L.J.G., analysis). Y.L. designed and fabricated solar cell samples, conducted the measurements, and performed data analysis. C.J. contributed to fabrication and characterization of the transparent electrode, outcoupling design, and data analysis. Y.Q. designed, fabricated, and characterized the antireflecting coating structure, and fabricated outcoupling layers. X.H. fabricated and measured solar cells. S.H. designed and developed DBR. L.L. and C.L. provided the materials. S.R.F. and L.J.G. supervised the project and analyzed data. All authors discussed the results and contributed to the manuscript.

Conflict of Interest

S.R.F. has an equity interest in one of the sponsors (UDC).

Keywords

nonfullerene acceptors, solar cells, transparent electronics

Received: May 17, 2019

Revised: July 7, 2019

Published online: August 16, 2019

- [1] C. J. Traverse, R. Pandey, M. C. Barr, R. R. Lunt, *Nat. Energy* **2017**, *2*, 849.
- [2] <http://www.iea-pvps.org/index.php?id=93>, National Survey Reports of PV Power Applications, **2017** (accessed: August 2019).
- [3] R. F. Bailey-Salzman, B. P. Rand, S. R. Forrest, *Appl. Phys. Lett.* **2006**, *88*, 233502.
- [4] R. R. Lunt, V. Bulovic, *Appl. Phys. Lett.* **2011**, *98*, 113305.
- [5] T. Ameri, G. Dennler, C. Waldauf, H. Azimi, A. Seemann, K. Forberich, J. Hauch, M. Scharber, K. Hingerl, C. J. Brabec, *Adv. Funct. Mater.* **2010**, *20*, 1592.
- [6] R. R. Lunt, *Appl. Phys. Lett.* **2012**, *101*, 043902.
- [7] R. Betancur, P. Romero-Gomez, A. Martinez-Otero, X. Elias, M. Maymo, J. Martorell, *Nat. Photonics* **2013**, *7*, 995.
- [8] C.-C. Chen, L. Dou, R. Zhu, C.-H. Chung, T.-B. Song, Y. B. Zheng, S. Hawks, G. Li, P. S. Weiss, Y. Yang, *ACS Nano* **2012**, *6*, 7185.
- [9] Q. Xue, R. Xia, C. J. Brabec, H.-L. Yip, *Energy Environ. Sci.* **2018**, *11*, 1688.
- [10] J. Sun, J. J. Jasieniak, *J. Phys. D: Appl. Phys.* **2017**, *50*, 093001.
- [11] C. Sun, R. Xia, H. Shi, H. Yao, X. Liu, J. Hou, F. Huang, H.-L. Yip, Y. Cao, *Joule* **2018**, *2*, 1816.
- [12] Y. Li, G. Xu, C. Cui, Y. Li, *Adv. Energy Mater.* **2018**, *8*, 1701791.
- [13] Q. Tai, F. Yan, *Adv. Mater.* **2017**, *29*, 1700192.
- [14] D. Shin, S.-H. Choi, *Coatings* **2018**, *8*, 329.
- [15] J. Meiss, F. Holzmueller, R. Gresser, K. Leo, M. Riede, *Appl. Phys. Lett.* **2011**, *99*, 193307.
- [16] K.-S. Chen, J.-F. Salinas, H.-L. Yip, L. Huo, J. Hou, A. K. Y. Jen, *Energy Environ. Sci.* **2012**, *5*, 9551.
- [17] C.-Y. Chang, L. Zuo, H.-L. Yip, Y. Li, C.-Z. Li, C.-S. Hsu, Y.-J. Cheng, H. Chen, A. K. Y. Jen, *Adv. Funct. Mater.* **2013**, *23*, 5084.
- [18] Y. Li, J.-D. Lin, X. Che, Y. Qu, F. Liu, L.-S. Liao, S. R. Forrest, *J. Am. Chem. Soc.* **2017**, *139*, 17114.
- [19] Y. Cui, C. Yang, H. Yao, J. Zhu, Y. Wang, G. Jia, F. Gao, J. Hou, *Adv. Mater.* **2017**, *29*, 1703080.
- [20] F. Liu, Z. Zhou, C. Zhang, J. Zhang, Q. Hu, T. Vergote, F. Liu, T. P. Russell, X. Zhu, *Adv. Mater.* **2017**, *29*, 1606574.
- [21] W. Wang, C. Yan, T. K. Lau, J. Wang, K. Liu, Y. Fan, X. Lu, X. Zhan, *Adv. Mater.* **2017**, *29*, 1701308.
- [22] T. Li, S. Dai, Z. Ke, L. Yang, J. Wang, C. Yan, W. Ma, X. Zhan, *Adv. Mater.* **2018**, *30*, 1705969.
- [23] Y. Xie, L. Huo, B. Fan, H. Fu, Y. Cai, L. Zhang, Z. Li, Y. Wang, W. Ma, Y. Chen, Y. Sun, *Adv. Funct. Mater.* **2018**, *28*, 1800627.
- [24] X. Ma, Z. Xiao, Q. An, M. Zhang, Z. Hu, J. Wang, L. Ding, F. Zhang, *J. Mater. Chem. A* **2018**, *6*, 21485.
- [25] J. Chen, G. Li, Q. Zhu, X. Guo, Q. Fan, W. Ma, M. Zhang, *J. Mater. Chem. A* **2019**, *7*, 3745.
- [26] J. Zhang, G. Xu, F. Tao, G. Zeng, M. Zhang, Y. Yang, Y. Li, Y. Li, *Adv. Mater.* **2019**, *31*, 1807159.
- [27] Y. Li, J. D. Lin, X. Liu, Y. Qu, F. P. Wu, F. Liu, Z. Q. Jiang, S. R. Forrest, *Adv. Mater.* **2018**, *30*, 1804416.
- [28] H. J. Snaith, *Energy Environ. Sci.* **2012**, *5*, 6513.
- [29] J. Q. Xi, J. K. Kim, E. F. Schubert, D. Ye, T. M. Lu, S.-Y. Lin, J. S. Juneja, *Opt. Lett.* **2006**, *31*, 601.
- [30] G. Xu, L. Shen, C. Cui, S. Wen, R. Xue, W. Chen, H. Chen, J. Zhang, H. Li, Y. Li, Y. Li, *Adv. Funct. Mater.* **2017**, *27*, 1605908.
- [31] J. Kettle, N. Bristow, T. K. N. Sweet, N. Jenkins, G. A. dos Reis Benatto, M. Jørgensen, F. C. Krebs, *Energy Environ. Sci.* **2015**, *8*, 3266.
- [32] T. Aernouts, P. Vanlaeke, W. Geens, J. Poortmans, P. Heremans, S. Borghs, R. Mertens, R. Andriessen, L. Leenders, *Thin Solid Films* **2004**, *451–452*, 22.
- [33] J.-Y. Lee, S. T. Connor, Y. Cui, P. Peumans, *Nano Lett.* **2008**, *8*, 689.
- [34] L. Hu, H. S. Kim, J.-Y. Lee, P. Peumans, Y. Cui, *ACS Nano* **2010**, *4*, 2955.
- [35] L. Hu, D. S. Hecht, G. Grüner, *Nano Lett.* **2004**, *4*, 2513.
- [36] M. W. Rowell, M. A. Topinka, M. D. McGehee, H.-J. Prall, G. Dennler, N. S. Sariciftci, L. Hu, G. Gruner, *Appl. Phys. Lett.* **2006**, *88*, 233506.
- [37] S. Bae, H. Kim, Y. Lee, X. Xu, J.-S. Park, Y. Zheng, J. Balakrishnan, T. Lei, H. Ri Kim, Y. I. Song, Y.-J. Kim, K. S. Kim, B. Özyilmaz, J.-H. Ahn, B. H. Hong, S. Iijima, *Nat. Nanotechnol.* **2010**, *5*, 574.
- [38] Z. Liu, P. You, S. Liu, F. Yan, *ACS Nano* **2015**, *9*, 12026.
- [39] WINDOW 4.0: Documentation of Calculation Procedures Report no. LBL-33943.